

Enhanced Charging/Discharging Process in Perovskite Active Light Source for High-Speed Visible-Light Communication

Haoyue Zhang, Yuru Tang, Chen Chen,* Meiqin Xiao, Jonghee Yang, Wei Zhang,* Chaochao Qin,* Ting Xiang, Long Xu, and Ping Chen*

Metal halide perovskites are promising light source materials for visible light communication (VLC) due to their excellent photoelectric properties and small resistance-capacitance time constant. However, previous reports mainly used perovskites as the passive light sources, which not only makes it susceptible to posterior excitation light sources, but also complex in the integration process. Herein, the quasi-2D PEA2Cs_{n-1}Pb_nBr_{3n+1} perovskite light-emitting diodes (PeLEDs) as an active light source in VLC link is demonstrated. It is found that the charging/discharging process of PeLEDs is an important factor governing the -3 dB bandwidth ($f_{-3 dB}$) of the VLC. To improve this, 3-sulfopropyl methacrylate potassium salt (SMPS) molecules are introduced into perovskite to simultaneously passivate deep and shallow energy level defects at grain boundaries. Additionally, the multiple quantum wells structures of PEA₂Cs_{n,1}Pb_nBr_{3n+1} are modified to be flat. At the optimal SMPS concentration, the maximum external quantum efficiency of PeLEDs reaches 21.5%. Meanwhile, the VLC achieves 3.2 MHz f_{.3 dB} with data transmission of 18.6 Mbps, which is the highest f_{-3 dB} in PeLEDs with the same active area. Hence, it provides a versatile method to improve the performance of VLC links based on active light sources and advances toward the goal of high-speed, energy-efficient and secure free communication.

1. Introduction

Visible light communication (VLC) is a wireless communication technology that enables information transmission by using

a light source with a fast on-off switching feature as a data source.[1-3] Light-emitting diodes (LEDs) are generally recognized as the most effective light sources for VLC,[1] because they not only satisfy the requirements of high brightness and low power consumption, but also possess high reaction sensitivity and preeminent modulation performance. Until now, LEDs applied into the VLC utilize various semiconducting materials including inorganics,[4] organics,[2] and colloid quantum dots (QDs).[3] Among the LEDs employing various emitter materials, recently metal halide perovskite (MHP)-based LEDs (PeLEDs) have emerged due to its excellent optical properties, demonstrating high color purity,[5] full-color luminescence[6] and high luminance efficiency.[7] More importantly, PeLEDs exhibit a small resistancecapacitance (RC) time constant[8,9] due to the low defect density[7,10] and high carrier mobility^[5,11] of the MHP. This allows them to render a very fast charging/discharging process for ultra-fast data transmission speeds. Therefore,

the PeLEDs highlight an exciting path toward the next generation of VLC.

The use of MHP in VLC has greatly gained attention, but so far, it has been mainly used as a passive light source. The

H. Zhang, M. Xiao, T. Xiang, L. Xu, P. Chen Chongqing key Laboratory of Micro&Nano Structure Optoelectronics School of Physical Science and Technology Southwest University

Chongqing 400715, China E-mail: pingchen@swu.edu.cn

Y. Tang, C. Chen School of Microelectronics and Communication Engineering

Chongqing University
Chongqing 400044, China
E-mail: c.chen@cqu.edu.cn

The ORCID identification number(s) for the author(s) of this article can be found under https://doi.org/10.1002/adom.202303051

DOI: 10.1002/adom.202303051

J. Yang

Institute for Advanced Materials and Manufacturing Department of Materials Science and Engineering University of Tennessee

Knoxville, TN 37996, USA

W. Zhang

Chongqing Institute of Green and Intelligent Technology

Chinese Academy of Sciences Chongqing 400714, China E-mail: zhangwei@cigit.ac.cn

C. Qin

Henan Key Laboratory of Infrared Materials and Spectrum Measures and Applications

School of Physics Henan Normal University Xinxiang 453007, China

E-mail: qinchaochao@htu.edu.cn

ADVANCED
OPTICAL
MATERIALS

21951071, 0, Downloaded from https://onlinelibrary.wiley.com/doi/10.1002adom.202303051 by Zhejjang University, Wiley Online Library on [13/12/2023]. See the Terms and Conditions (https://onlinelibrary.wiley.com/rerms-and-conditions) on Wiley Online Library for rules of use; OA articles are governed by the applicable Creative Commons Licensean Conditions (https://onlinelibrary.wiley.com/rerms-and-conditions) on Wiley Online Library for rules of use; OA articles are governed by the applicable Creative Commons Licensean Conditions (https://onlinelibrary.wiley.com/rerms-and-conditions) on Wiley Online Library for rules of use; OA articles are governed by the applicable Creative Commons Licensean Conditions (https://onlinelibrary.wiley.com/rerms-and-conditions) on Wiley Online Library for rules of use; OA articles are governed by the applicable Creative Commons Licensean Conditions (https://onlinelibrary.wiley.com/rerms-and-conditions) on Wiley Online Library for rules of use; OA articles are governed by the applicable Creative Commons Licensean Conditions (https://onlinelibrary.wiley.com/rerms-and-conditions) on Wiley Online Library for rules of use; OA articles are governed by the applicable Creative Commons Licensean Conditions (https://onlinelibrary.wiley.com/rerms-and-conditions) on Wiley Online Library for rules of use; OA articles are governed by the applicable Creative Commons (https://onlinelibrary.wiley.com/rerms-and-conditions) on Wiley Online Library for rules of use; OA articles are governed by the applicable Creative Commons (https://onlinelibrary.wiley.com/rerms-and-conditions) on Wiley Online Library for rules of use; OA articles are governed by the applicable Creative Commons (https://onlinelibrary.wiley.com/rerms-and-conditions) on Wiley Online Library for rules of use; OA articles are governed by the applicable Creative Commons (https://onlinelibrary.wiley.com/rerms-and-conditions) on the applicable Creative Commons (https://onlinelibrary.wiley.com/rerms-and-conditions) on the applicable Creative

MHP passive light sources were referential to the phosphors ones, where the emissive layer is used as the color converter and stimulated by the posterior LEDs. For example, Zang et al.[12] introduced green DDAB-CsPbBr₃/SiO₂ and red InAgZnS QDs composite material as a color conversion layer to synthesize white light on a blue LEDs chip with -3 dB bandwidth ($f_{-3 \text{ dB}}$) of 1.5 MHz. Tian et al.[13] used a blue GaN micro-LEDs exciting yellow emitting $CsPbBr_{1.8}I_{1.2}$ YQDs for a high $f_{-3 dB}$ of 73 MHz white VLC. Fu et al.[14] prepared CsPb(Br_x/I_{1-x})₃ nanocrystals (NCs)- and CsPbI₃ NCs-PMMA films with the $f_{-3 dB}$ of 347 and 822 MHz, respectively. Osman M. Bakr et al. [15] treated CsPbBr₃ NCs with red phosphor light, and combined it into white light system which showed $f_{-3 dB}$ of 491 MHz. Despite the high $f_{-3 dB}$ of passive light sources, some drawbacks are introduced. First, the light output by passive light is usually white when the posterior excitation light is not fully absorbed by perovskite films. Thus, the light cannot fully represent the VLC capacity of perovskites.^[14] In addition, the complex integration process of passive light increases the cost of devices.^[16]

One of the feasible routes to solve the issues above is operating the PeLEDs as an active light source directly driven by high-frequency pulse voltage bias. However, the $f_{-3\,dB}$ of passive light source platform (serval hundreds MHz) still outperforms that of active light source (kHz–MHz). The primary reason for lower $f_{-3\,dB}$ of PeLEDs could be attributed to the tricky control over the perovskite defect density in the thin film system (can surge over 10^{19} cm $^{-3}$), $^{[17]}$ particularly stemming from the nature of solution processing. This subsequently hinders the fast and frequent charging/discharging process of PeLEDs governing the $f_{-3\,dB}$ in VLC. Thus, due to the lack of a thorough understanding of defect control and effective strategies for improving the charging/discharging process in PeLEDs, their applications for active light source have not been extensively explored so far.

In this study, we develop high_performance PeLEDs employing a surface-engineered quasi-2D PEA2Cs, Pb, Br3n+1 MHP as an active light source for VLC. The dual-passivation 3-sulfopropyl methacrylate potassium salt (SMPS) are incorporated into quasi-2D $PEA_2Cs_{n-1}Pb_nBr_{3n+1}$ MHP, which comprehensively passivate the deep- and shallow-level defects in perovskite through their concurrent binding actions based on Lewis acid-base interaction and cation-vacancy: binding of S=O with uncoordinated Pb²⁺ and filling the Cs⁺ vacancy with K⁺. In addition to the defect suppression, homogenization of quasi-2D phase distributions with suppression of small n phases is realized by SMPS, which flattens the MQWs structure, reduces the energetic disorders, and thereby manifests more efficient charge transport. Consequently, the device performances are improved with respective maximum external quantum efficiency (EQE_{max}) and maximum luminescence (L_{max}) of \approx 21.5% and \approx 29 860 cd m⁻².

We found that the SMPS-incorporation strategy is also beneficial to realize fast and frequent charging/discharging process under high-frequency pulse voltage operation, which greatly improves the VLC performance by directly using the PeLEDs as an active light source. Specifically, over twofold improvement of $f_{-3 \text{ dB}}$, reaching 3.2 MHz, is achieved by the PeLEDs employing SMPS-modified perovskite emission layer, which is, to the best of our knowledge, the highest $f_{-3 \text{ dB}}$ of PeLEDs reported so far (among those with active areas ranging to 1–10 mm²). By using an orthogonal frequency division multiplexing (OFDM) modu-

lation with adaptive bit loading, the achievable data rate reaches 18.6 Mbps in VLC system. This study systematically visualizes the impact of defect passivation on the VLC performances employing PeLEDs active light source. The comprehensive defect passivation strategy demonstrated in this work provides practical insights for the development of high-speed, energy-efficient and wearable VLC systems in the future.

2. Results and Discussion

The SMPS (Figure 1a) are dissolved in the perovskite precursor solution as an additive. Sulfonyl group (O=S=O)[18] and potassium ions (K⁺)^[19] in SMPS molecules play an important role in passivation perovskite defects to improve luminescence and communication capacities of PeLEDs. Under the same bias voltage, the SMPS-modified device shows the higher bright green Electroluminescence (EL) (peak centered at 512 nm) compared to the control device without involving notable spectral shift (Figure S1, Supporting Information). The current density-luminescencevoltage (I-L-V) curves of the SMPS-modified and the control device are shown in Figure 1b,c, and the parameters are summarized in Table S1 (Supporting Information). The J-V characteristics indicate that the current density of the SMPS-modified device is improved compared to the control device. The SMPSmodified devices show L_{max} of \approx 29 860 cd m⁻² and EQE_{max} of up to 21.5%. These are substantially higher than those for the control devices ($L_{\rm max}$, \approx 9109 cd m $^{-2}$, EQE $_{\rm max}$, 10.2%). Note that there are considerable EQE roll-offs in the PeLEDs, stemming from the quasi-2D MHPs structure (Figure 1c). It has been known that quasi-2D MHPs are deemed to suffer from substantial Auger recombination by excessive local accumulation of excited-state carriers.[20] This in turn causes notable luminescence quenching and EQE roll-off, particularly at the high charge injection regime.

In addition, we compare the EL half-lifetime ($T_{50\text{-}EL}$) of the PeLEDs measured under DC and high-frequency pulse voltage operation conditions of 100 kHz and 3 MHz, respectively. As shown in Figure 1d and Figure S2 (Supporting Information), at the relatively low frequency of 100 kHz, the stability of PeLEDs is significantly improved compared with DC operation. This is due to the suppressed Joule heating and charge accumulation. [21] Further increasing the frequency to 3 MHz starts to compromise the PeLEDs stability. This can be ascribed to the rebuilding of Joule heating in the device, attributed to the insufficient time to cool (relax) the temperature elevated at the last pulse-operation cycle. Even so, the decays of $T_{50\text{-}EL}$ under 3 MHz are still slower than those of DC conditions, indicating great potentials of our PeLEDs for the VLC applications with fast and frequent charging/discharging process.

Figure 1e indicates VLC link using PeLEDs as an active light source. The detailed experimental setup is shown in Figure S3 (Supporting Information). The electrical-optical-electrical (EOE) frequency response is shown in Figure 1f for obtaining the $\rm f_{-3~dB}$. Compared with the control devices, over twofold enhancements of the $\rm f_{-3~dB}$, from 1.5 to 3.2 MHz, are observed from the SMPS-modified devices

To explore the mechanism enabling substantial increase of $f_{-3~\mathrm{dB}}$ in the SMPS-modified devices, we investigate the transient EL (Tr-EL) of the PeLEDs under 6.0 V, 100 kHz square voltage

21951071, 0, Downloaded from https://onlinelibrary.wiley.com/doi/10.1002/adom.202303051 by Zhejiang University, Wiley Online Library on [13/12/2023]. See the Terms and Conditions (https://onlinelibrary.wiley.com/terms

-and-conditions) on Wiley Online Library for rules of use; OA articles are governed by the applicable Creative Commons License

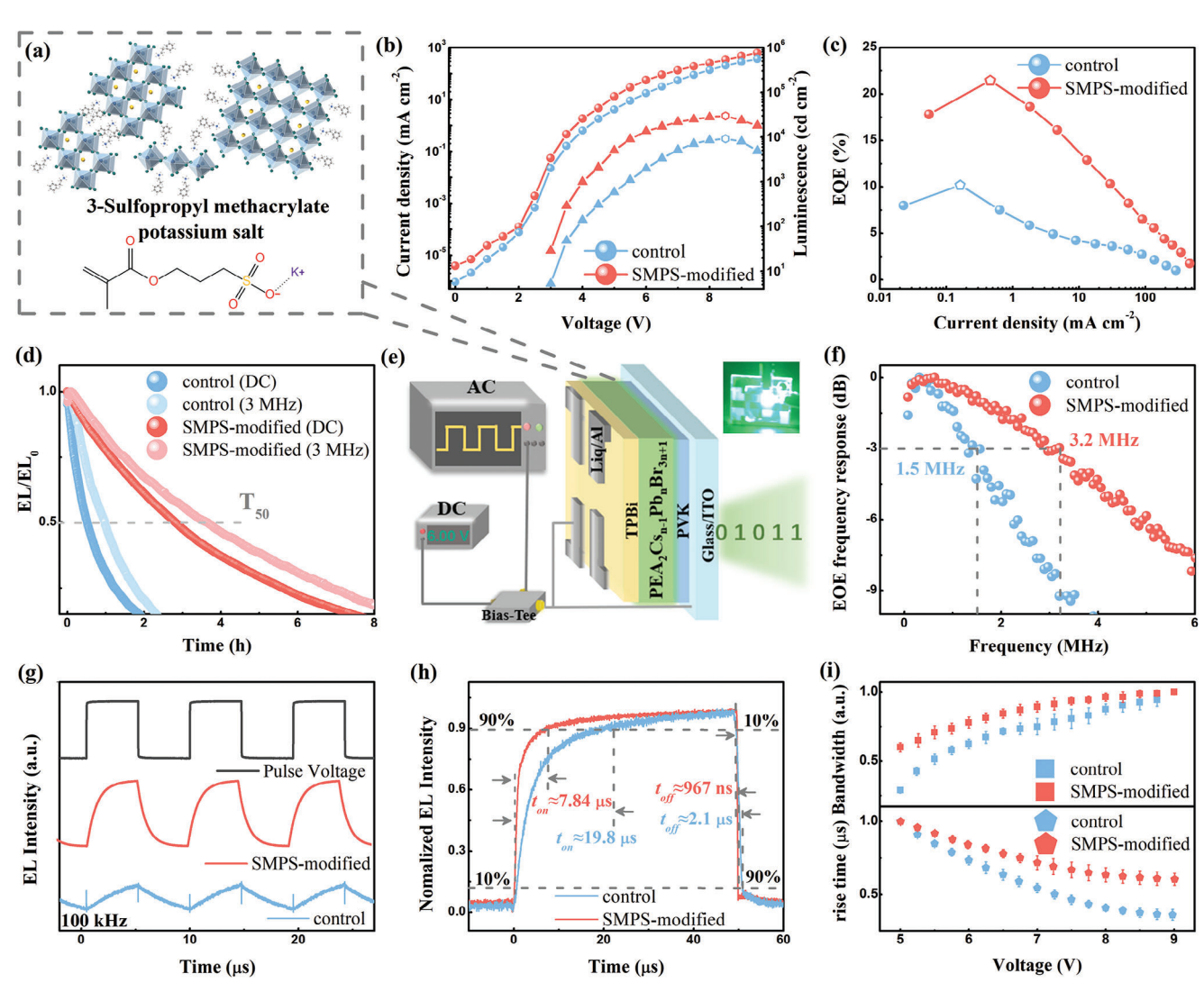


Figure 1. a) Structure of quasi-2D perovskite and chemical structures of SMPS. J-L-V characteristics of PeLEDs including b) J-V, L-V and c) EQE-J characteristics. d) EL half-lifetime (T_{50-EL}) of the PeLEDs measured under DC and high frequency pulse voltage operation conditions of 3 MHz, respectively. e) Schematic diagram VLC system based on active PeLEDs light source. f) EOE frequency response of the control and the SMPS-modified PeLEDs. Tr-EL of the control and the SMPS-modified PeLEDs under 6.0 V, g) 100 kHz square pulse and h) 10 kHz square pulse. i) The $f_{-3 dB}$ and rise time of the control and the SMPS-modified PeLEDs vary with voltage, and there are three for each device. The $f_{-3 dB}$ and rise time data are divided by their maximum values, respectively.

pulse with duty circle of 50%, as shown in Figure 1g. For the SMPS-modified devices, upon turn-on state, the Tr-EL shows a sharp rise and reaches to a saturation level. When the pulse is turned off, the Tr-EL intensity is dropped rapidly to an off-state. Collectively, the augmented luminance with fast on/off dynamics of SMPS-modified PeLEDs result in a remarkable intensity difference ($E_{\rm gap}$) between the turn-on and turn-off states. Such remarkable $E_{\rm gap}$ indicates an evident difference between 0 and 1 signals during the communication, which is critical for high $f_{-3~{\rm dB}}$. $^{[16]}$ In contrast, the control device exhibits slow Tr-EL rise and fall dynamics that significantly limits the maximum Tr-EL intensity. This subsequently results in relatively smaller $E_{\rm gap}$ that compromises a poor signal-to-noise ratio (SNR), making difficult to distinguish the 0 and 1 signals and thus, limiting the $f_{-3~{\rm dB}}$ of VLC.

We further explore the Tr-EL on/off dynamics by using a 10 kHz-pulsed bias (Figure 1h), quantifying the 10-to-90% rise and fall times ($t_{\rm on}$ and $t_{\rm off}$, respectively)[22] of the PeLEDs. The SMPS-modified devices exhibit \approx 2.5- and threefolds faster turn-on and off rates with a respective $t_{\rm on}$ and $t_{\rm off}$ of 7.84 µs and 697 ns, compared to the control devices ($t_{\rm on}$ and $t_{\rm off}$ of 19.8 and 2.1 µs, respectively). The faster Tr-EL on/off dynamics of the SMPS-modified device is attributed to faster charging/discharging process. We further explore the dependence of $t_{\rm -3\,dB}$ and $t_{\rm on}$ on the DC voltages, as shown in Figure 1i. It is noted that $t_{\rm on}$ decreases but $t_{\rm -3\,dB}$ increases with increasing a DC bias, higher bias not only increases the amount of injected carriers enhancing luminance but also accelerates charge injection kinetics (i.e., faster drift velocity). [16] We observed that the SMPS-modified devices exhibit shorter $t_{\rm on}$ and larger $t_{\rm -3\,dB}$, attributed to faster

21951071, 0, Downloaded from https://onlinelibrary.wiley.com/doi/10.1002/adom.202303051 by Zhejiang University, Wiley Online Library on [13/12/2023]. See the Terms and Conditions (https://onlinelibrary.wiley.com/rerns-a-d-conditions) on Wiley Online Library for rules of use; OA articles are governed by the applicable Creative Commons Licensense and Conditions (https://onlinelibrary.wiley.com/rerns-a-d-conditions) on Wiley Online Library for rules of use; OA articles are governed by the applicable Creative Commons Licensense and Conditions (https://onlinelibrary.wiley.com/rerns-a-d-conditions) on Wiley Online Library for rules of use; OA articles are governed by the applicable Creative Commons Licensense and Conditions (https://onlinelibrary.wiley.com/rerns-a-d-conditions) on Wiley Online Library for rules of use; OA articles are governed by the applicable Creative Commons Licensense and Conditions (https://onlinelibrary.wiley.com/rerns-a-d-conditions) on Wiley Online Library for rules of use; OA articles are governed by the applicable Creative Commons Licensense and Conditions (https://onlinelibrary.wiley.com/rerns-a-d-conditions) on Wiley Online Library for rules of use; OA articles are governed by the applicable Creative Commons Licensense and Conditions (https://onlinelibrary.wiley.com/rerns-a-d-conditions) on Wiley Online Library for rules of use; OA articles are governed by the applicable Creative Commons (https://onlinelibrary.wiley.com/rerns-a-d-conditions) on Wiley Online Library for rules of use; OA articles are governed by the applicable Creative Commons (https://onlinelibrary.wiley.com/rerns-a-d-conditions) on Wiley Online Library for rules of use; OA articles are governed by the applicable Creative Commons (https://onlinelibrary.wiley.com/rerns-a-d-conditions) on the applicable Creative Commons (https://onlinelibrary.wiley.com/rerns-a-d-conditions) on the applicable Creative Commons (https://onlinelibrary.wiley.com/rerns-a-d-conditions) on the applicable Creative Commons (https://onlinelibrary.wiley

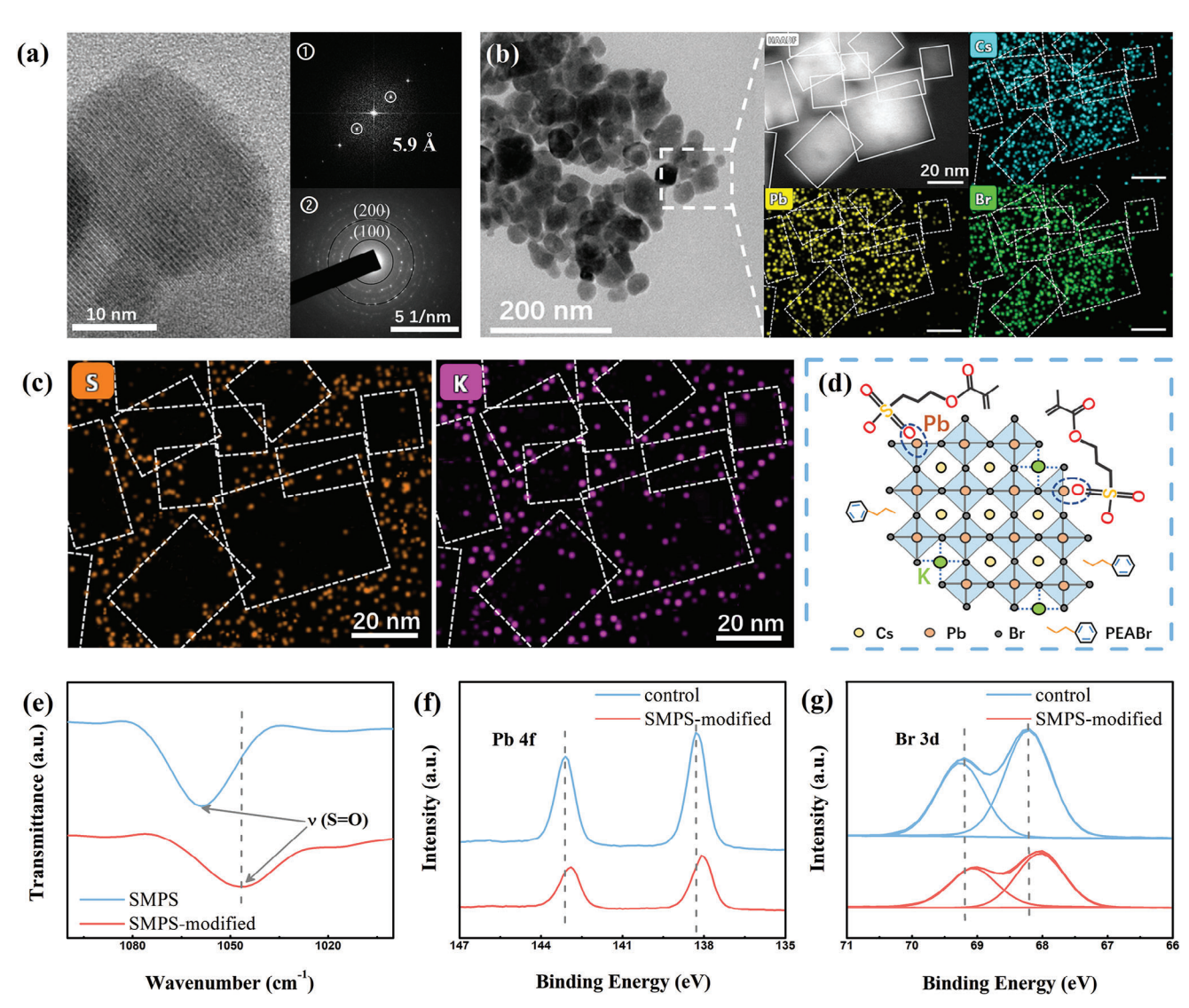


Figure 2. a) TEM image of the SMPS-modified films. The inset ① and ② show the FFT images and SAED patterns of the films. b) The STEM image and the STEM-EDS mappings show the distribution of Cs, Pb and Br elements in the SMPS-modified films. c) STEM-EDS mappings show the distribution of S and K element in the SMPS-modified films. d) Schematic illustration of the dual-passivation by SMPS at perovskite grain boundaries. e) FTIR spectroscopy of SMPS and SMPS-modified thin films. XPS f) Pb 4f, and g) Br 3d core-level spectra for control and SMPS-modified thin films.

charging/discharging process by reduced defect density. The energy bands of the perovskite thin films are investigated by ultraviolet photo-electron spectroscopy (UPS) and UV-vis absorption. As shown in Figure S4 and Table S2 (Supporting Information), the conduction band (CB) of the SMPS-modified film slightly declines from -2.96 to -3.01 eV while the valence band (VB) of both films undergoes negligible redshift from -5.32 to -5.35 eV. Such little changes in the VB and CB rule out the impact of energy band alignments, solely attributing the improved PeLEDs performances to the comprehensive defect passivation by SMPS.

The passivation effects of SMPS on the trap densities of perovskite are investigated in **Figure 2**. The transmission electron microscopy (TEM) is used to characterize the crystal structure of SMPS-modified perovskite. As depicted in Figure 2a, the SMPS-modified perovskite crystallites exhibit a highly crystal-

lized cubic structure. Moreover, the fast Fourier transform (FFT) images show the lattice fringes with d spacing of 5.9 Å (the inset ① of Figure 2a), which is consistent with the reported lattice constants of $PEA_2Cs_{n-1}Pb_nBr_{3n+1}$. [23,24] The crystal structural is further revealed by selected-area electron diffraction (SAED), as shown in the inset 2, where diffraction spots are assigned to (100) and (200) planes. [25] These observations are in good agreement with the X-ray diffraction (XRD) patterns in Figure S5 (Supporting Information). To gain better insights into the spatial distribution of SMPS around the perovskites, energy-dispersive X-ray spectroscopy (EDS) elemental mapping are performed to the SMPS-modified perovskite crystallites in scanning TEM (STEM) measurement. As shown in Figure 2b,c, it is observed that Cs, Pb, and Br elements are concentrated on the perovskite interiors, whereas the S and K signals mainly surround the edges of the perovskite crystallites. This verifies that the SMPS

ADVANCED OPTICAL MATERIALS 21951071, 0, Downloaded from https://onlinelibrary.wiley.com/doi/10.1002/adom.202303051 by Zhejjang University, Wiley Online Library on [13/122023]. See the Terms and Conditions (https://onlinelibrary.wiley.com/rerms-and-conditions) on Wiley Online Library for rules of use; OA articles are governed by the applicable Creative Commons Licensean Conditions (https://onlinelibrary.wiley.com/rerms-and-conditions) on Wiley Online Library for rules of use; OA articles are governed by the applicable Creative Commons Licensean Conditions (https://onlinelibrary.wiley.com/rerms-and-conditions) on Wiley Online Library for rules of use; OA articles are governed by the applicable Creative Commons Licensean Conditions (https://onlinelibrary.wiley.com/rerms-and-conditions) on Wiley Online Library for rules of use; OA articles are governed by the applicable Creative Commons Licensean Conditions (https://onlinelibrary.wiley.com/rerms-and-conditions) on Wiley Online Library for rules of use; OA articles are governed by the applicable Creative Commons Licensean Conditions (https://onlinelibrary.wiley.com/rerms-and-conditions) on Wiley Online Library for rules of use; OA articles are governed by the applicable Creative Commons Licensean Conditions (https://onlinelibrary.wiley.com/rerms-and-conditions) on Wiley Online Library for rules of use; OA articles are governed by the applicable Creative Commons (https://onlinelibrary.wiley.com/rerms-and-conditions) on Wiley Online Library for rules of use; OA articles are governed by the applicable Creative Commons (https://onlinelibrary.wiley.com/rerms-and-conditions) on Wiley Online Library for rules of use; OA articles are governed by the applicable Creative Commons (https://onlinelibrary.wiley.com/rerms-and-conditions) on Wiley Online Library for rules of use; OA articles are governed by the applicable Creative Commons (https://onlinelibrary.wiley.com/rerms-and-conditions) on the applicable Creative Commons (https://onlinelibrary.wiley.com/rerms-and-conditions) on the applicable Creative

molecules mainly passivate the perovskite surfaces and are thereby located at the grain boundaries.

At the grain boundaries of quasi-2D MHP, a dual-surface passivation mechanism of SMPS molecules is considered, as schematically depicted in Figure 2d. First, SMPS can passivate deep level surface defects originating from undercoordinated Pb²⁺ ions at the grain boundaries.^[26] Both sulfoxide (SO₃), carbonyl (C=O) groups in SMPS molecules, containing lone pairs of electrons, are feasible to form moderate dative bonds with the undercoordinated Pb²⁺, thereby passivating the defects.^[27] Second, SMPS can also passivate shallow level traps originating from Cs⁺ vacancies, caused by the rapid crystallization and growth process.^[28] The smaller ionic radii of potassium ions (K⁺) than that of Cs⁺ -1.38 and 1.67 Å, respectively – allows them to accumulate at the grain boundaries to passivate these defects by filling the vacancies.^[29]

Experimentally, the dual-passivation action of SMPS upon incorporation into MHP is confirmed by the Fourier transform infrared (FTIR) (Figure 2e) and X-ray photoelectron spectroscopy (XPS) (Figure 2f,g). The full spectroscopies of the FTIR are provided in Figure S6a (Supporting Information). Figure 2e and Figure S6b (Supporting Information) show the stretching mode of sulfonyl ($\approx 1058 \text{ cm}^{-1}$; v(S=O)) and carbonyl ($\approx 1720 \text{ cm}^{-1}$; ν (C=O)) bonds, respectively. Upon incorporation into MHP, the sulfonyl peak exhibits a shift to the lower wavenumber of 1045 cm⁻¹, evidencing the coordination action of SO₃ with the undercoordinated Pb²⁺. [30] In contrast, the shift of carbonyl peak is not observed upon the SMPS incorporation, suggesting the contribution of C=O to Pb²⁺ passivation is negligible. This observation suggests the S=O has a stronger electron-withdrawing capacity compared to the C=O, leading to more effective passivation of the Pb²⁺ vacancies by S=O.^[18] Figure 2f exhibits Pb 4f core-level XPS spectra of the MHP films, showing a significantly shift to lower binding energy. This confirms the Lewis acid-based interaction between the S=O and uncoordinated Pb2+. Such shift toward lower binding energy is also observed for the Br 3d spectrum in Figure 2g, which may come from the variation of the Pb²⁺...Br⁻ interactions^[27] and/or the K⁺...Br⁻ interactions.^[31] Therefore, XPS measurement of the control films with KBr (Figure S7, Supporting Information) is further conducted to demonstrate the contribution of K+. For the films with KBr, the Lewis passivation of Pb²⁺ is ruled out but only with K⁺ passivation. The Br 3d peak also shifts to the low binding energy, indicating K⁺ does replace the vacancy of Cs⁺ and has an effect on Br⁻. These results confirm that SMPS molecules can effectively passivate the deep and shallow level defects of perovskite through Lewis passivation of Pb $^{2+}$ by S=O and occupying vacancy of Cs $^{+}$ by K $^{+}$.

To characterize the trap density of states (tDOS) in shallow and deep level, the thermal admittance spectroscopy (TAS) technique is employed. The tDOS can be calculated by capacitance-frequency (C–F) measurements (Figure S8, Supporting Information) through Equation (1)^[32]:

$$N_T (E_{\omega}) = \frac{V_{bi}}{qW} \frac{dC_p}{d\omega} \frac{\omega}{k_B T}$$
 (1)

where width of the space charge region (W) and built-in potential ($V_{\rm bi}$) are extracted from the capacitance–voltage (C-V) curve (Figure S9, Supporting Information). C, ω , and k_BT are capac-

itors, frequency, and thermal energy, respectively. Compared to control device, the SMPS-modified device shows one or two orders of magnitude lower tDOS in the shallow-trap region (0.30–0.40 eV)^[33] by Cs⁺ vacancies and the deep-trap region (0.50–0.55 eV)^[34] by undercoordinated Pb²⁺, respectively, as shown in **Figure 3a**. The space charge-limited current (SCLC) technique^[35] is further provided for defect density by Equation (2):

$$n_{trap} = \frac{2V_{TFL}\varepsilon_r\varepsilon_0}{eL^2} \tag{2}$$

where onset voltage (V_{TFL}) is the trap filling limit voltage, e is the electronic charge, L is the thickness of perovskite films, e_r and e_0 are the relative permittivity and vacuum permittivity. For hole-only devices with SMPS-modified perovskite layer (Figure 3b), the $V_{\rm TFL}$ of devices is significantly reduced from ≈ 1.6 to 0.8 V, indicating the trap density ($n_{\rm trap}$) of holes is reduced from $\approx 3.35 \times 10^{18}$ to 1.59×10^{18} cm⁻³ (Table S3, Supporting Information). Similarly, we can see the $n_{\rm trap}$ of electrons (Figure S10, Supporting Information) is reduced from $\approx 2.95 \times 10^{18}$ to 1.31×10^{18} cm⁻³. Therefore, both $n_{\rm trap}$ of electrons and holes are reduced by SMPS.

We further perform time-resolved photoluminescence (TRPL) measurement in Figure 3c, which can be fitted by the following three-exponential functions (3)^[36]:

$$I(t) = I_0 + A_1 \exp(-t/\tau_1) + A_2 \exp(-t/\tau_2) + A_3 \exp(-t/\tau_3)$$
 (3)

where A_1 , A_2 , and A_3 are amplitudes, and τ_1 , τ_2 , and τ_3 are fast, medium and slow decay lifetimes constants. The fitting parameters are extracted in Table S4 (Supporting Information). Obviously, the SMPS-modified film show longer PL average lifetime ($\tau_{ave} = \frac{A_1\tau_1 + A_2\tau_2 + A_3\tau_3}{A_1 + A_2 + A_3}$) of 11.62 ns, compared with 3.36 ns for control film, attributed to the suppression of nonradiative recombination process by dual-surface passivation with SMPS.

Subsequently, electrochemical impedance spectroscopy (EIS) is conducted to examine the charge transport and recombination behaviors. The PeLEDs are measured in dark condition under AC excitation from 1 MHz to 10 Hz, as shown in Figure 3d. As shown in the inset, the equivalent circuit model consists of a series resistance (R_s), a recombination resistance ($R_{\rm rec}$) and a parallel capacitance (C).^[37] $R_{\rm s}$ is attributed to resistances from device interfaces, and $R_{\rm rec}$ is associated with the recombination resistance of the perovskite layer.^[38] According to the fitting parameters in Table S5 (Supporting Information), the SMPS-modified device has lower $R_{\rm s}$ and $R_{\rm rec}$ than the control device. The reduced $R_{\rm s}$ facilitates electronic charge injection and transport,^[39] and the significant reduction of $R_{\rm rec}$ indicates that the SMPS-modified devices achieve higher radiation recombination rate due to reduced trap density.^[38]

In addition to the defect suppression, the n phases of the excited states can be redistributed by SMPS. Figure 3e,f shows the scanning electron microscope (SEM) images of the control and SMPS-modified films, respectively. Compared to the inhomogeneous grain sizes distribution of control films, the grain sizes in the SMPS-modified films become homogeneous. Although the grain sizes are seemed to be reduced upon the modification in the corresponding SEM images, we note that the grain sizes in the SMPS-modified film still show a nominal value >50 nm, far larger than the nominal Bohr radii of perovskites (3–6 nm)^[40]

21951071, 0, Downloaded from https://onlinelibrary.wiley.com/doi/10.1002/adom.202303051 by Zhejiang University, Wiley Online Library on [13/12/2023]. See the Terms and Condition of the Conditio

and-conditions) on Wiley Online Library for rules of use; OA articles are governed by the applicable Creative Commons License

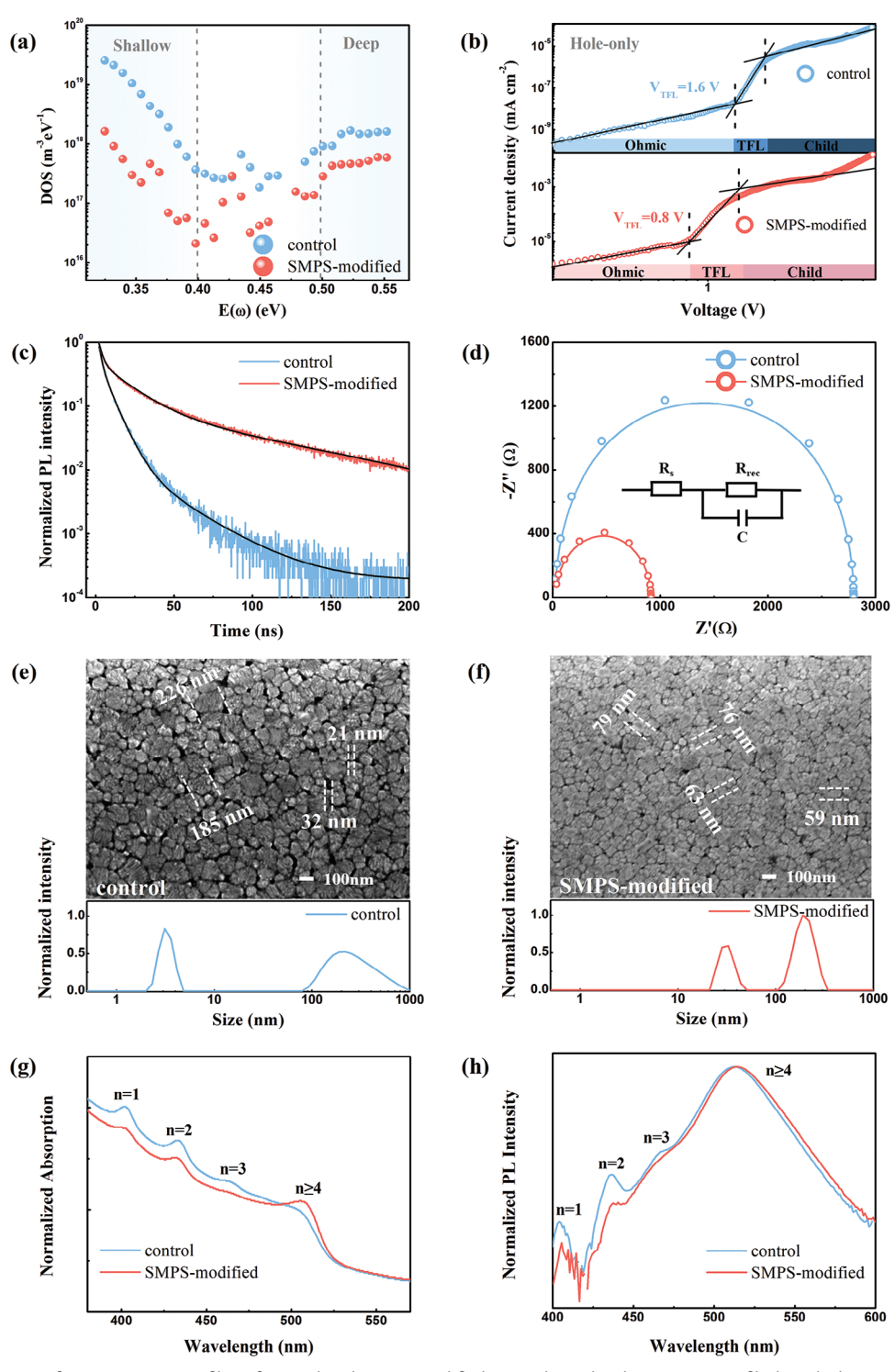


Figure 3. a) Trap density of states (tDOS) profiles of control and SMPS-modified perovskites. b) The J–V curves of hole-only devices with the control and SMPS-modified films c) Normalized TRPL decays of the control and SMPS-modified perovskite films. d) Nyquist plots of the control and SMPS-modified devices from EIS measurements (at applied bias of 3.5 V). Top-view SEM images and DLS spectra of e) the control and f) the SMPS-modified perovskite films. g) The steady-state UV–vis absorption and h) PL spectra of control and SMPS-modified perovskite films.

21951071, 0, Downloaded from https://onlinelibrary.wiley.com/doi/10.1002adom.202303051 by Zhejjang University, Wiley Online Library on [13/12/2023]. See the Terms and Conditions (https://onlinelibrary.wiley.com/rerms-and-conditions) on Wiley Online Library for rules of use; OA articles are governed by the applicable Creative Commons Licensean Conditions (https://onlinelibrary.wiley.com/rerms-and-conditions) on Wiley Online Library for rules of use; OA articles are governed by the applicable Creative Commons Licensean Conditions (https://onlinelibrary.wiley.com/rerms-and-conditions) on Wiley Online Library for rules of use; OA articles are governed by the applicable Creative Commons Licensean Conditions (https://onlinelibrary.wiley.com/rerms-and-conditions) on Wiley Online Library for rules of use; OA articles are governed by the applicable Creative Commons Licensean Conditions (https://onlinelibrary.wiley.com/rerms-and-conditions) on Wiley Online Library for rules of use; OA articles are governed by the applicable Creative Commons Licensean Conditions (https://onlinelibrary.wiley.com/rerms-and-conditions) on Wiley Online Library for rules of use; OA articles are governed by the applicable Creative Commons Licensean Conditions (https://onlinelibrary.wiley.com/rerms-and-conditions) on Wiley Online Library for rules of use; OA articles are governed by the applicable Creative Commons (https://onlinelibrary.wiley.com/rerms-and-conditions) on Wiley Online Library for rules of use; OA articles are governed by the applicable Creative Commons (https://onlinelibrary.wiley.com/rerms-and-conditions) on Wiley Online Library for rules of use; OA articles are governed by the applicable Creative Commons (https://onlinelibrary.wiley.com/rerms-and-conditions) on Wiley Online Library for rules of use; OA articles are governed by the applicable Creative Commons (https://onlinelibrary.wiley.com/rerms-and-conditions) on the applicable Creative Commons (https://onlinelibrary.wiley.com/rerms-and-conditions) on the applicable Creative

- the dimension where the quantum confinement starts to affect the perovskite electronic structure. In addition, dynamic light scattering (DLS) characterizations show that the formation of small colloidal particles (size: 3-5 nm) - potentially responsible for the formation of low-n (i.e., n = 1-3) 2D MHP phases - are greatly suppressed upon SMPS modification even in the precursor states. This can subsequently increase the population of high-n (n≥4) phase in the perovskite films after crystallization, manifesting the redshifts in both absorption and PL spectra (Figure 3g,h). These observations suggest that the formation of small n phases are rigorously regulated by SMPS incorporation, thereby leaving homogeneous, large-n rich MHP phase distribution in the resulting film.

Steady-state UV-vis absorption and PL spectra are shown in Figure 3g,h, respectively. Absorption peaks at ≈400, 432, 463 and 505 nm correspond to absorptions of n = 1, 2, 3 and $n \ge 4$ phases.[41,42] For the SMPS-modified films, the peaks of 402 (n = 1), 433 (n = 2), and 464 (n = 3) nm are suppressed, while the peak of 509 nm is significantly enhanced. Such redistribution of n phases can be also seen in PL spectroscopies where the emission from small n phases is inhibited, while the emission from large n phase is enhanced in SMPS-modified films. The homogenized phase distribution where the formation of the small n 2D phases upon SMPS incorporation subsequently results in flattened MQW energy level landscape, which is majorly composed of the narrow-bandgap MHP.

To explore the details of the structure of MQWs and energy transfer characteristics through the MQWs, transient absorption (TA) spectroscopies are carried out. Four distinctive ground-state bleaching (GSB) peaks are observed around 405, 435, 466 and 516 nm in the control films as shown in **Figure 4a**, which correspond to excited-states n = 1, 2, 3 and $n \ge 4$, respectively. The photogenerated excited states are initially formed at n = 1 (405 nm) phase. Then, the GSB signals of n = 2, n = 3, and $n \ge 4$ are generated in sequence. It is observed that the $n\geq 4$ phase is gradually formed when small n phases of n = 1, 2, 3 diminishes, indicating that a charge transfer takes place from small n phases to large n phase. [43] Compared to control devices, the GSB signals of n = 1, 2, 3 in SMPS-modified devices are almost negligible (Figure 4b), leaving dominant GSB signal of n≥4. To understand more details of the carrier transportation, the decay kinetics of each GSB are extracted in Figure 4c,d, and the multi-exponential function Equation (4) is used to fit the GSB signals^[44]:

$$\Delta A (\tau) = A_1 e^{(-t/\tau_1)} + A_2 e^{(-t/\tau_2)} + A_3 e^{(-t/\tau_3)} + B_1 e^{(-t/\tau_{et})}$$
(4)

where A_1 , A_2 , A_3 , and B_1 are amplitudes, τ_1 is the fast decay time constant assigned to the carrier transferring from small n phases to large n phases in perovskite films, τ_2 and τ_3 represent the slow decay time constant, and τ_{et} is the formation time constant. The fitting parameters are compared in the Table \$6 (Supporting Information). In control films, the fast decay time τ_1 of n = 2 and n= 3 phases are 0.66 and 5.47 ps, respectively, followed by the carrier funneling into $n \ge 4$ phase for the radiative recombination. In contrast, the τ_1 of n = 2 and n = 3 phases in SMPS-modified perovskite films are shortened to 0.31 and 3.16 ps, indicating more efficient energy transfer from the small n phases to the large n phase. [45] Besides, the τ_{et} of SMPS-modified perovskite thin films is 0.70 ps, smaller than that of control thin films (0.94 ps), verify-

Adv. Optical Mater. 2023, 2303051

ing the improvement of charge transfer by regulated formation of small n phases.

Moreover, the change of defect density and the MOWs structure will also benefit the charging/discharging process for VLC, as shown in Figure 4e. In the control devices with high defect density and the inhomogeneous MQWs structure, the defect states capture or scatter the free carriers during the charge transport.[46] Moreover, given the principle of electroluminescence in PeLEDs where the holes and electrons respectively injected from the hole transport layer (HTL) and electron transport layer (ETL) should reach large n perovskite phases upon charge transport, carriers should overcome the energy barrier of ΔE_{VR} or ΔE_{CR} when they transport across the intermediate-large n phase to small n phases prior to finally reach to the large n phase responsible for desired EL emission.[47] Those defect-induced and energetic disorders manifest significant charge trappingdetrapping events when the external electric field is employed. Subsequently, this notably slows down the charging/discharging process, as reflected as longer $t_{\rm on}$ and $t_{\rm off}$ during Tr-EL operation (Figure S11, Supporting Information). For SMPS-modified devices, the density of defect states are significantly reduced and the energy barriers of ΔE_{VB} or ΔE_{CB} in MQWs are largely mitigated by homogenized phase distribution. This significantly suppress the charge trapping-detrapping events, thereby resulting in accelerating fast charging/discharging process, which are conducive to efficient VLC.

Finally, we investigate the effects of SMPS concentrations on the device efficiency. As concentration of the SMPS increases from 0 to 1.2 mg mL⁻¹, the defect density gradually decreases (Figures S12 and S13, Supporting Information) and the MQWs structure gradually flattens (Figures S14–S16, Supporting Information), leading to improved device performances (Figure S17, Supporting Information). However, the device performance declines at the SMPS concentration of 1.8 mg mL⁻¹, which is likely due to excessive non-conductive SMPS that inhibits carrier injection and transportation.[48]

The VLC responses of PeLEDs are shown in Figure 5. In the optimal concentration of 1.2 mg mL $^{-1}$, \approx 3.2 MHz $f_{-3 \text{ dB}}$ is obtained from the EOE frequency response. To the best of our knowledge, this is the highest $f_{-3 dB}$ record for active light PeLEDs among the devices with similar active areas, as summarized in Table \$7 (Supporting Information).[16,49-51] Clear and wide eye diagram of a 1 MHz square wave signal is observed, indicating the high signal transmission quality. Moreover, the VLC system with a modulation bandwidth of 10 MHz exhibits a high received SNR of more than 15 dB above the $f_{-3 dB}$. To deeply explore the achievable data rate, we apply OFDM modulation with adaptive bit loading in the system.^[12] The constellation diagrams available with PeLEDs include binary phase shift keying (BPSK), 4-ary quadrature amplitude modulation (4-QAM), 8-QAM, and 16-QAM, 32-QAM, and 64-QAM. The transmission data rate realized by the VLC system available with PeLEDs can reach 18.6 Mbps, which is approximately sixfold of the measured $f_{-3 \text{ dB}}$. The VLC responses of PeLEDs with different concentration of SMPS are also discussed. Similar to the trend of device performance, the communication performance of PeLEDs also present a trend of increasing first and then decreasing with SMPS concentration. Specifically, the $f_{-3 \text{ dB}}$ of PeLEDs containing 0, 0.6, 1.2 and 1.8 mg mL⁻¹ SMPS are 1.5, 2.5, 3.2 and 2.1 MHz, respectively (Figure 5a-c). The other

21951071, 0, Downloaded from https://onlinelibrary.wiley.com/doi/10.1002/adom.202303051 by Zhejiang University, Wiley Online Library on [13/12/2023]. See the Terms and Conditional Condition of the Condition of the Conditional Condition of the Cond

conditions) on Wiley Online Library for rules of use; OA articles are governed by the applicable Creative Commons License

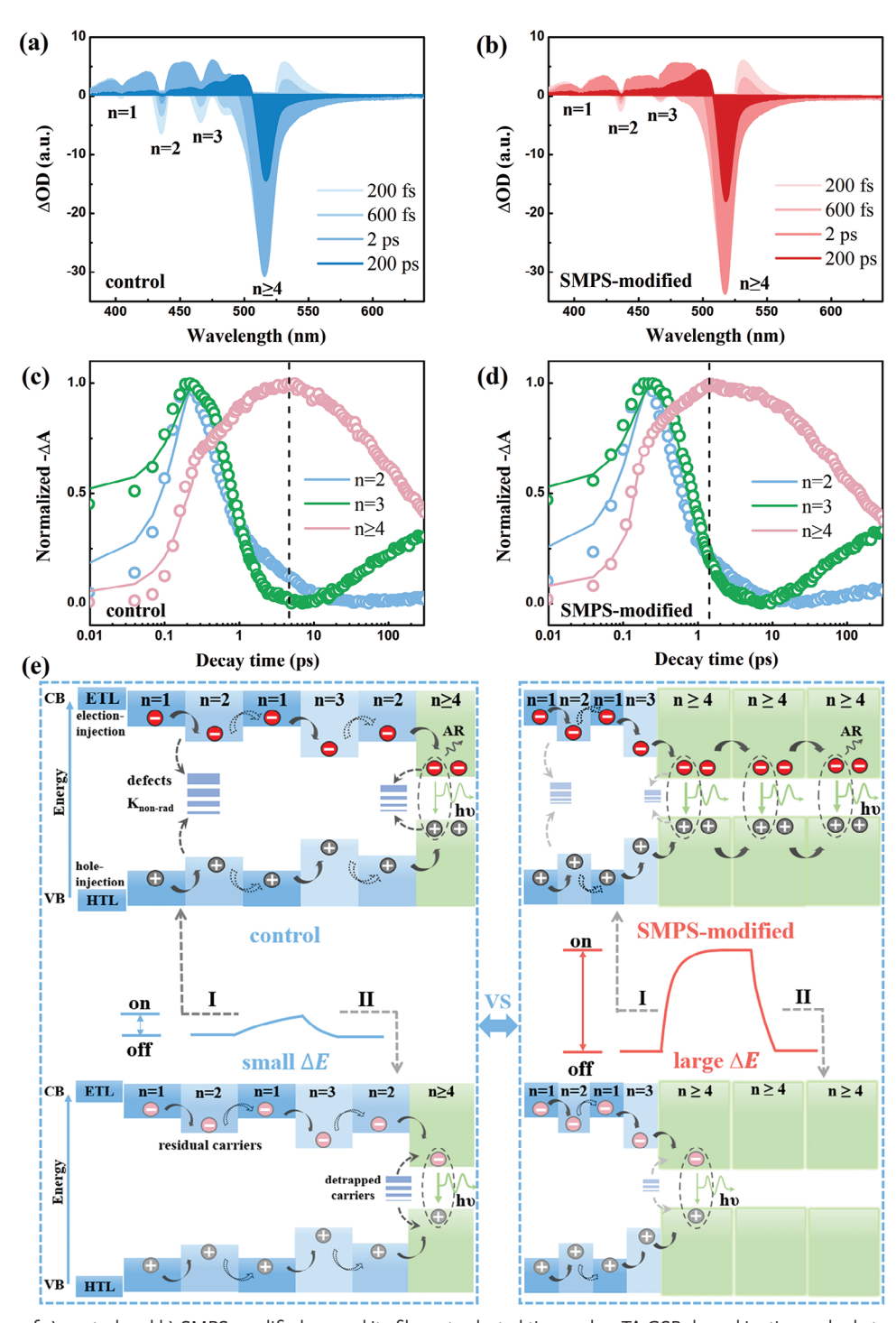


Figure 4. TA spectra of a) control and b) SMPS-modified perovskite films at selected timescales. TA GSB decay kinetics probed at selected wavelengths for c) control and d) SMPS-modified perovskite films, respectively. e) Schematic illustration of passivated defects and flatted MQWs energy structure by a multifunctional SMPS.

constellation diagrams that can be loaded for each concentration are shown in Figures S18–S21 (Supporting Information), and the corresponding transmission data rates are 4.5, 12.5 and 8.4 Mbps, respectively. We also attribute this trend to enhancement of the charging/discharging process by SMPS molecules at low concentrations, but it is restricted at high concentrations.

To further highlight the advantage of the PeLEDs, we also explore the VLC performances of the flexible PeLEDs (Figure S22, Supporting Information), which are fabricated on the flexible PEN substrate. At the normal and bending (curvature with a ≈ 2 cm radius) conditions, the flexible PeLEDs demonstrate respective $f_{-3~\text{dB}}$ of ≈ 0.9 and 0.5 MHz (Figures S23 and S24,

21951071, 0, Downloaded from https://onlinelibrary.wiley.com/doi/10.1002/adom.202303051 by Zhejiang University, Wiley Online Library on [13/12/2023]. See the Terms and Conditions (https://onlinelibrary.wiley.com/terms

-and-conditions) on Wiley Online Library for rules of use; OA articles are governed by the applicable Creative Commons License

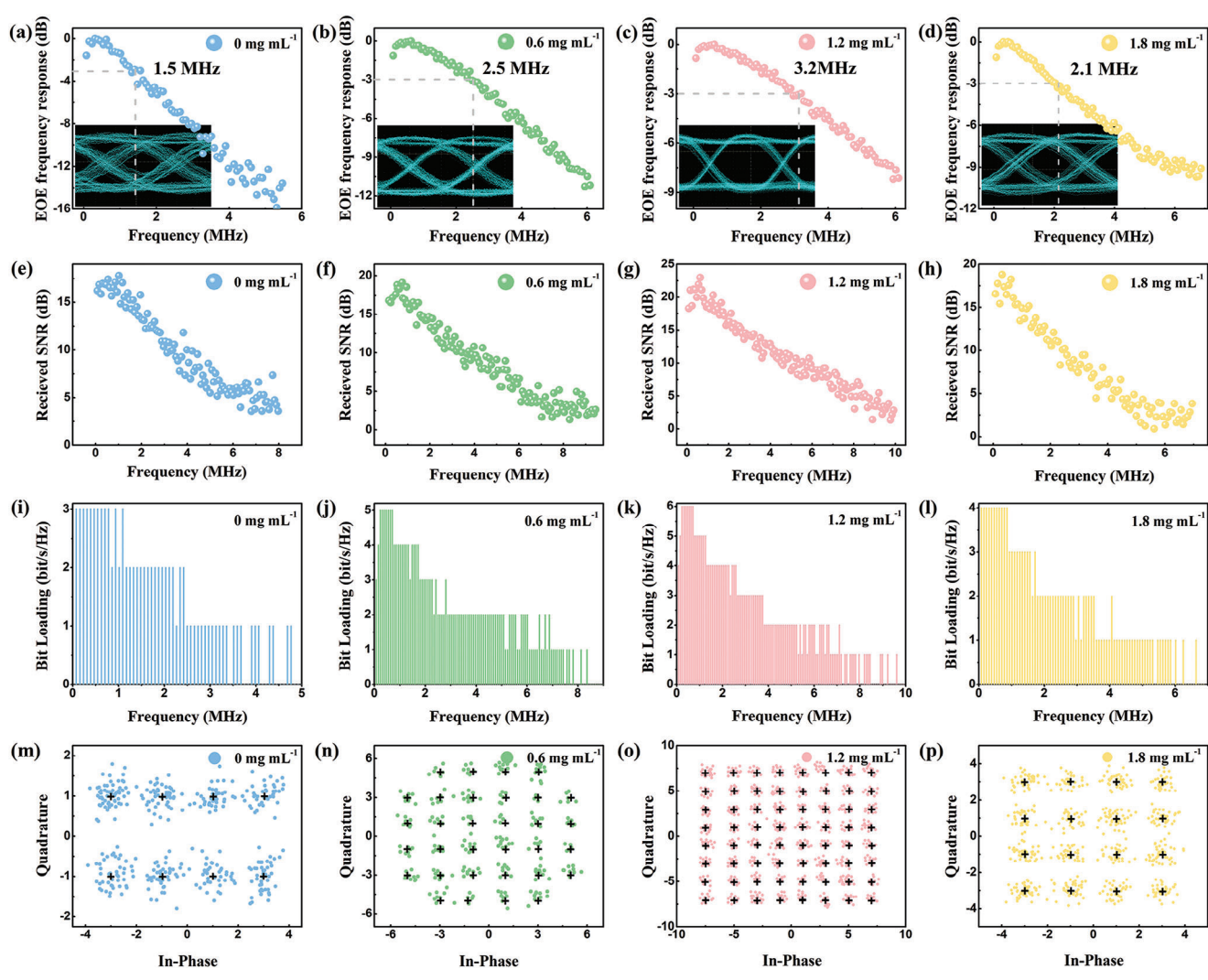


Figure 5. a-d) EOE frequency response, e-h) received SNR, and i-l) bit loading profile of the VLC system based on PeLEDs with different concentration of SMPS. m) The corresponding constellation diagrams of 8-QAM base on the PeLEDs with the concentration of SMPS is 0 mg mL $^{-1}$. n) The corresponding constellation diagrams of 32-QAM base on the PeLEDs with the concentration of SMPS is 0.6 mg mL⁻¹. o) The corresponding constellation diagrams of 64-QAM base on the PeLEDs with the concentration of SMPS is 1.2 mg mL⁻¹. p) The corresponding constellation diagrams of 16-QAM base on the PeLEDs with the concentration of SMPS is 1.8 mg mL^{-1} .

Supporting Information). Note the $f_{-3\;dB}$ decrease for the bended devices could be attributed to the increased defect densities and larger void sizes between grain boundaries induced by the mechanical force, further aggravating the charging/discharging process. Nevertheless, we highlight that these demonstrations suggest great potential of flexible PeLEDs in wearable VLC, which still has a very large room to be developed to achieve high $f_{-3 dB}$ flexible PeLEDs in the future.

3. Conclusion

In summary, the high-efficiency quasi-2D PEA2Cs_{n-1}Pb_nBr_{3n+1} perovskite has been fabricated for the VLC as an active light source. It is found that the $f_{-3 dB}$ of VLC link strongly depends on the charging/discharging process of PeLEDs. Therefore, SMPS is used as a dual-passivation to reduce the defect density at both deep and shallow levels, and redistribute the n phases for a flat energy structure in MOWs. Finally, the concentration of SMPS molecules is adjusted to maximize device efficiency and VLC performance. At the optimal concentration of 1.2 mg mL⁻¹, the EQE_{max} of the PeLEDs reaches 21.5%. The $f_{-3 dR}$ of VLC reaches 3.2 MHz, representing the highest $f_{-3 \text{ dB}}$ of PeLEDs in the same active area. After OFDM modulation with adaptive bit loading, the transmission data rate of VLC system can reach 18.6 Mbps. These results not only demonstrate the substantial impact of defect passivation in efficient and high-frequency pulse voltage operations, but also pave the way to overcome the current challenges and thereby replace the existing technologies with the promising PeLEDs active light source in VLC link platform. [52,53] For examples, there are two strategies to improve the communication capability by using PeLEDs. First, the micro-PeLEDs can reducing the parasitic capacitance of the device, [16] and the nearly linear increase of the $f_{-3\,dB}$ with decreasing device area. In addition, single crystal thin film PeLEDs can significantly

21951071, 0, Downloaded from https://onlinelibrary.wiley.com/doi/10.1002adom.202303051 by Zhejjang University, Wiley Online Library on [13/12/2023]. See the Terms and Conditions (https://onlinelibrary.wiley.com/rerms-and-conditions) on Wiley Online Library for rules of use; OA articles are governed by the applicable Creative Commons Licensean Conditions (https://onlinelibrary.wiley.com/rerms-and-conditions) on Wiley Online Library for rules of use; OA articles are governed by the applicable Creative Commons Licensean Conditions (https://onlinelibrary.wiley.com/rerms-and-conditions) on Wiley Online Library for rules of use; OA articles are governed by the applicable Creative Commons Licensean Conditions (https://onlinelibrary.wiley.com/rerms-and-conditions) on Wiley Online Library for rules of use; OA articles are governed by the applicable Creative Commons Licensean Conditions (https://onlinelibrary.wiley.com/rerms-and-conditions) on Wiley Online Library for rules of use; OA articles are governed by the applicable Creative Commons Licensean Conditions (https://onlinelibrary.wiley.com/rerms-and-conditions) on Wiley Online Library for rules of use; OA articles are governed by the applicable Creative Commons Licensean Conditions (https://onlinelibrary.wiley.com/rerms-and-conditions) on Wiley Online Library for rules of use; OA articles are governed by the applicable Creative Commons (https://onlinelibrary.wiley.com/rerms-and-conditions) on Wiley Online Library for rules of use; OA articles are governed by the applicable Creative Commons (https://onlinelibrary.wiley.com/rerms-and-conditions) on Wiley Online Library for rules of use; OA articles are governed by the applicable Creative Commons (https://onlinelibrary.wiley.com/rerms-and-conditions) on Wiley Online Library for rules of use; OA articles are governed by the applicable Creative Commons (https://onlinelibrary.wiley.com/rerms-and-conditions) on the applicable Creative Commons (https://onlinelibrary.wiley.com/rerms-and-conditions) on the applicable Creative

improve its $f_{-3 dB}$ due to its low defect density and superior charge transfer properties.^[54] We believe that combining emerging active PeLEDs with VLC links will lead to achieve practical high-speed data transmission for next-generation communications. Also, the comprehensive defect passivation strategy shown in this work provides fundamental insights into the development of efficient, sustainable, and ubiquitous realization of PeLED-based VLC system in the future.

4. Experimental Section

Materials: Cesium bromide (CsBr, >99.999%) was purchased from Alfa Aesar. Lead bromide (PbBr₂, >99.99%) and phenethylammonium bromide (PEABr, >99.5%) were purchased from Xi'an Yuri Solar. 3-Sulfopropyl methacrylate potassium salt(SMPS, >98%)was purchased from Macklin. Potassium bromide (KBr, >99.99%), Poly (9-vinylcarbazole) (PVK, average $M_w \approx 90~000$), dimethyl sulfoxide (DMSO, >99.8%, GC), and chlorobenzene (CB, >99.5%, GC) were purchased from Aladdin. All chemicals were used as received without further purification.

Perovskite Precursor Solution: The perovskite precursor solution was prepared by dissolving CsBr, PbBr₂ and PEABr at a molar ratio of 1.2:1:0.3 in the DMSO solution to give an overall concentration of 10 wt.%. Then, the perovskite precursor solution was stirred at room temperature for 10 h under nitrogen atmosphere. The SMPS was added to the perovskite precursor solution in 0.6, 1.2, and 1.8 mg mL⁻¹. The mixed solution was stirred at room temperature for 3 h under nitrogen atmosphere before

PeLED Fabrication: The structure of the PeLEDs was indium tin oxide (ITO)-coated glass/ Poly(N-vinylcarbazole) (PVK) (30 nm)/perovskite (50 nm)/ 1,3-tris(1-phenyl-19H-benzo[d]- imidazol-2-yl)benzene (TPBi) (50 nm)/8-hydroxyquinolinatolithium (Liq) (2.5 nm)/Al (100 nm). The structures of the hole-only and electron-only devices were ITO/PVK (30 nm)/perovskite (50 nm)/ Molybdenum trioxide (MoO₃) (50 nm)/Al (100 nm) and ITO/ZnO (30 nm)/perovskite (50 nm)/TPBi (50 nm)/Lig (2.5 nm)/Al (100 nm), respectively. The PVK solution was spin-coated onto UV/ozone-treated ITO substrates at 4000 rpm for 60 s and then annealed at 150°C for 15 min. Then, the perovskite layer was deposited by spincoating precursor solution on ITO/PVK substrates at 4000 rpm for 60 s. The above were carried out under nitrogen atmosphere. Finally, functional layers of TPBi, Liq and Al were sequentially evaporated through a shadow mask (active device area 6 mm 2) at a pressure of 3 \times 10 $^{-4}$ Pa using an LN-1123SC organic/metal composite multisource evaporation system. All devices were encapsulated by hot melt adhesive with a glass cover for further measurements.

Characterizations: The FTIR measurements were conducted by Fourier transform infrared spectrometer (Nicolet iS 10). The TEM was measured using JELO JEM-2100Plus. To obtain the nanocrystals from the thin films, the samples were immersed into chlorobenzene to dissolve the underlying organic layers. Then, perovskite nanocrystals were peeled off from ITO substrate. Finally, perovskite nanocrystals were transferred by drop-casting the chlorobenzene suspension onto the carbon-coated copper grids for TEM testing. SEM measurement was performed by JEOL JSM-7100F. The crystal structures were determined by XRD patterns characterized by a TD-3500 instrument. A Kratos Axis Supra+ system was used for XPS analysis of Cs 3d, Pb 4f, and Br 3d chemical states. The excitation source was Al $K\alpha$ (1486.6 eV). The steady-state PL was measured with an Ocean Optics USB2000+ fiber optic spectrometer. The EL spectra were measured by a PR670 spectroscopy colorimeter. The steady-state UV-vis absorption was recorded using a Shimadzu UV-2600 spectrophotometer. The TA spectroscopy was performed on a pump-probe system (Helios, Ultrafast System LLC) coupled with an amplified femtosecond laser system (Coherent) under ambient conditions. Using a picosecond pulsed diode laser (EPL-375) with a maximum average power of $\approx\!\!2~\mu\text{W},$ the PL lifetime was measured with the Edinburgh Instruments (LifeSpec-II) spectrometer. The EIS was measured on a CHI660D electrochemical work station (CH In-

strument Inc.). A 2 mV voltage amplitude was applied at an applied bias voltage of 3.5 V with frequencies between 1 MHz and 10 Hz under dark conditions. The Z-view software was used to fit the impedance spectra to obtain the impedance parameters. The capacitance-voltage (C-V) measurements were recorded using a Paios parameter analyzer at 1 kHz with an AC amplitude of 20 mV. The capacitance-frequency (C-F) measurements were performed using Paios parameter analyzer with the frequency range from 10 Hz to 10 MHz and an AC amplitude of 20 mV. The J-L-V characteristics of PeLEDs were carried out by Keithley 2400 sourcemeter and luminance meter (KONICA, LS-110) Colorimeter. The VLC system is illustrated in Figure S3 (Supporting Information). The AC electrical signal generated by the arbitrary waveform generator (Tektronix AFG31000 series) and the 8.0 V DC generated by the Keithley 2400 precision power were combined via a bias-T (ZFBT-6GW+). Then the signal was employed to the PeLEDs. After that, the optical signals emitted by the PeLEDs propagate through the space of 0.5 m and are gathered by the lens to the PDA modules (C12702 series) for reception. After converting the optical signal into an electrical signal, the resulting electrical signal was sampled via a digital storage oscilloscope (DSO) (Tekronix MDO4054-3). The output data was processed offline via MATLAB, so as to realize the measurement of VLC.

Supporting Information

Supporting Information is available from the Wiley Online Library or from the author.

Acknowledgements

This work was financially supported by Fundamental Research Funds for the Natural Science Foundation Project of CQ CSTC (Grant nos. CSTB2022NSCQ-MSX0438), the Natural Science Foundation of Chongqing China (Grant No. cstc2021jcyj-jqX0031), Interdiscipline Team Project under auspices of "Light of West" Program in Chinese Academy of Sciences (Grant no. xbzg-zdsys-202106), the Young Scholar of Regional Development Program in Chinese Academy of Sciences (Grant No. 2021), and the Graduate Student Research Innovation Project of Chongqing (Grant nos. CYS23186). The authors also acknowledge Prof. Qunliang Song and Dr. Cunyun Xu from the Institute for Clean Energy and Advanced Materials, Southwest University for their kind helps in EIS measurements.

Conflict of Interest

The authors declare no conflict of interest.

Author Contributions

H.Z. carried out the device fabrication and characterizations and wrote the first draft of the manuscript. Y.T. provides the MATLAB program and helped VLC measurements. C.C. provides the VLC system setup and made major revisions to the manuscript. M.X. helped in device fabrications and analyzed the J-V characteristics. J.Y. proof read the manuscript. W.Z. carried out the TEM measurements and conceived the project funding. C.Q. carried out the TA measurements. T.X. analyzed the TEM and TA data. L.X. helped organizing the graphic figures. P.C. conceived the idea and project funding, supervised the work, and made major revisions to the manuscript. All authors contributed to manuscript preparation and dis-

Data Availability Statement

The data that support the findings of this study are available from the corresponding author upon reasonable request.

21951071, 0, Downloaded from https://onlinelibrary.wiley.com/doi/10.1002/adom.202303051 by Zhejiang University, Wiley Online Library on [13/12/2023]. See the Terms and Conditions (https://onlinelibrary.wiley.com/terms

and-conditions) on Wiley Online Library for rules of use; OA articles are governed by the applicable Creative Commons License

Keywords

-3 dB bandwidth, active light sources, light emitting diodes, quasi-2D perovskite, visible light communication

> Received: November 29, 2023 Published online:

- [1] A. Ren, H. Wang, W. Zhang, J. Wu, Z. Wang, R. V. Penty, I. H. White, Nat. Electron. 2021, 4, 559.
- [2] A. Minotto, P. A. Haigh, L. G. Lukasiewicz, E. Lunedei, D. T. Gryko, I. Darwazeh, F. Cacialli, Light Sci. Appl. 2020, 9, 70.
- [3] H. Xiao, X. Xiao, D. Wu, R. Wang, K. Wang, K. S. Chiang, IEEE Trans. Electron Devices 2019, 66, 4805.
- [4] D. Karunatilaka, F. Zafar, V. Kalavally, R. Parthiban, IEEE Commun. Surv. Tutorials 2015, 17, 1649.
- [5] L. Zhang, C. Sun, T. He, Y. Jiang, J. Wei, Y. Huang, M. Yuan, Light Sci. Appl. 2021, 10, 61.
- [6] X.-K. Liu, W. Xu, S. Bai, Y. Jin, J. Wang, R. H. Friend, F. Gao, Nat. Mater. 2021, 20, 10.
- [7] Z. Liu, W. Qiu, X. Peng, G. Sun, X. Liu, D. Liu, Z. Li, F. He, C. Shen, Q. Gu, F. Ma, H.-L. Yip, L. Hou, Z. Qi, S.-J. Su, Adv. Mater. 2021, 33, 2103268.
- [8] L. Dou, Y. Yang, J. You, Z. Hong, W.-H. Chang, G. Li, Y. Yang, Nat. Commun. 2014, 5, 5404.
- [9] Z. S. Wang, F. Ebadi, B. Carlsen, W. C. H. Choy, W. Tress, Small Methods 2020, 4, 2000290.
- [10] C. Ran, J. Xu, W. Gao, C. Huang, S. Dou, Chem. Soc. Rev. 2018, 47, 4581.
- [11] T. He, S. Li, Y. Jiang, C. Qin, M. Cui, L. Qiao, H. Xu, J. Yang, R. Long, H. Wang, M. Yuan, Nat. Commun. 2020, 11, 1672.
- [12] X. Li, W. Cai, H. Guan, S. Zhao, S. Cao, C. Chen, M. Liu, Z. Zang, Chem. Eng. J. 2021, 419, 129551.
- [13] S. Mei, X. Liu, W. Zhang, R. Liu, L. Zheng, R. Guo, P. Tian, ACS Appl. Mater. Interfaces 2018, 10, 5641.
- [14] Z. Wang, Z. Wei, Y. Cai, L. Wang, M. Li, P. Liu, R. Xie, L. Wang, G. Wei, H. Y. Fu, ACS Appl. Mater. Interfaces 2021, 13,
- [15] I. Dursun, C. Shen, M. R. Parida, J. Pan, S. P. Sarmah, D. Priante, N. Alyami, J. Liu, M. I. Saidaminov, M. S. Alias, A. L. Abdelhady, T. K. Ng, O. F. Mohammed, B. S. Ooi, O. M. Bakr, ACS Photonics 2016, 3, 1150.
- [16] C. Bao, W. Xu, J. Yang, S. Bai, P. Teng, Y. Yang, J. Wang, N. Zhao, W. Zhang, W. Huang, F. Gao, Nat. Electron. 2020, 3, 156.
- [17] Y. Zhou, Z. Yang, Q. Huang, Y. Ye, B. Ye, Z. Shen, W. Wu, Z. Zeng, Z. Hong, Z. Meng, H. Hong, S. Ye, Z. Cheng, Q. Lan, J. Wang, Y. Chen, H. Zhang, T. Guo, F. Li, Y. Chen, Z. Weng, Org. Electron. 2023, 118,
- [18] C. Song, X. Li, Y. Wang, S. Fu, L. Wan, S. Liu, W. Zhang, W. Song, J. Fang, J. Mater. Chem. A 2019, 7, 19881.
- [19] Y. Liu, Y. Gao, M. Lu, Z. Shi, W. W. Yu, J. Hu, X. Bai, Y. Zhang, Chem. Eng. J. 2021, 426, 130841.
- [20] Y. Jiang, M. Cui, S. Li, C. Sun, Y. Huang, J. Wei, L. Zhang, M. Lv, C. Qin, Y. Liu, M. Yuan, Nat. Commun. 2021, 12, 336.
- [21] S. Yu, J. Hu, H. Zhang, G. Zhao, B. Li, Y. Xia, Y. Chen, ACS Photonics **2022**, 9, 1852.
- [22] C. Hosokawa, H. Tokailin, H. Higashi, T. Kusumoto, Appl. Phys. Lett. 1992. 60. 1220.
- [23] J. Si, Y. Liu, Z. He, H. Du, K. Du, D. Chen, J. Li, M. Xu, H. Tian, H. He, D. Di, C. Lin, Y. Cheng, J. Wang, Y. Jin, ACS Nano 2017, 11, 11100.
- [24] P. Vashishtha, M. Ng, S. B. Shivarudraiah, J. E. Halpert, Chem. Mater. 2019, 31, 83.

- [25] Y. Shang, G. Li, W. Liu, Z. Ning, Adv. Funct. Mater. 2018, 28, 1801193.
- [26] B. Chen, P. N. Rudd, S. Yang, Y. Yuan, J. Huang, Chem. Soc. Rev. 2019, 48. 3842.
- [27] L. Kong, X. Zhang, Y. Li, H. Wang, Y. Jiang, S. Wang, M. You, C. Zhang, T. Zhang, S. V. Kershaw, W. Zheng, Y. Yang, Q. Lin, M. Yuan, A. L. Rogach, X. Yang, Nat. Commun. 2021, 12, 1246.
- [28] J. Guo, J. Sun, L. Hu, S. Fang, X. Ling, X. Zhang, Y. Wang, H. Huang, C. Han, C. Cazorla, Y. Yang, D. Chu, T. Wu, J. Yuan, W. Ma, Adv. Energy Mater. 2022, 12, 2200537.
- [29] C. Li, A. Wang, L. Xie, X. Deng, K. Liao, J.-A. Yang, T. Li, F. Hao, J. Mater. Chem. A 2019, 7, 24150.
- [30] B. Guo, R. Lai, S. Jiang, L. Zhou, Z. Ren, Y. Lian, P. Li, X. Cao, S. Xing, Y. Wang, W. Li, C. Zou, M. Chen, Z. Hong, C. Li, B. Zhao, D. Di, Nat. Photonics 2022, 16, 637.
- [31] L. Wang, G. Wang, Z. Yan, J. Qiu, C. Jia, W. Zhang, C. Zhen, C. Xu, K. Tai, X. Jiang, S. Yang, Sol. RRL 2020, 4, 2000098.
- [32] K. Liu, Y. Luo, Y. Jin, T. Liu, Y. Liang, L. Yang, P. Song, Z. Liu, C. Tian, L. Xie, Z. Wei, Nat. Commun. 2022, 13, 4891.
- [33] J.-F. Liao, W.-Q. Wu, J.-X. Zhong, Y. Jiang, L. Wang, D.-B. Kuang, J. Mater. Chem. A 2019, 7, 9025.
- [34] Y. Jiang, C. Qin, M. Cui, T. He, K. Liu, Y. Huang, M. Luo, L. Zhang, H. Xu, S. Li, J. Wei, Z. Liu, H. Wang, G.-H. Kim, M. Yuan, J. Chen, Nat. Commun. 2019, 10, 1868.
- [35] T. Li, T. Xiang, M. Wang, W. Zhang, J. Shi, M. Shao, T. Xu, M. Ahmadi, X. Wu, Z. Gao, L. Xu, P. Chen, Laser Photonics Rev. 2021, 15,
- [36] T. Xiang, T. Li, M. Wang, W. Zhang, M. Ahmadi, X. Wu, T. Xu, M. Xiao, L. Xu, P. Chen, Nano Energy 2022, 95, 107000.
- [37] Y. Yu, R. Liu, C. Liu, X.-L. Shi, H. Yu, Z.-G. Chen, Adv. Energy Mater. 2022. 12. 2201509.
- [38] H. Zhang, F. Ye, W. Li, R. S. Gurney, D. Liu, C. Xiong, T. Wang, ACS Appl. Energy Mater. 2019, 2, 3336.
- [39] Y. Zhong, G. Liu, Y. Su, W. Sheng, L. Gong, J. Zhang, L. Tan, Y. Chen, Angew. Chemie.-Int. Ed. 2022, 61, e202114588.
- [40] L. Polavarapu, B. Nickel, J. Feldmann, A. S. Urban, Adv. Energy Mater. **2017**. 7. 1700267.
- Y. F. Ng, S. A. Kulkarni, S. Parida, N. F. Jamaludin, N. Yantara, A. Bruno, C. Soci, S. Mhaisalkar, N. Mathews, Chem. Commun. 2017, 53, 12004.
- [42] M. Xiao, T. Xiang, D. Kim, M. Wang, W. Zhang, M. Ahmadi, T. Li, X. Wu, L. Xu, P. Chen, ACS Appl. Mater. Interfaces 2022, 14, 45352.
- [43] J. Guo, Z. Shi, J. Xia, K. Wang, Q. Wei, C. Liang, D. Zhao, Z. Zhang, S. Chen, T. Liu, S. Mei, W. Hui, G. Hong, Y. Chen, G. Xing, Small 2021, 17, 2100560.
- [44] L. Yang, Y. Zhang, J. Ma, P. Chen, Y. Yu, M. Shao, ACS Energy Lett. 2021, 6, 2386.
- [45] X. Yu, T. Liu, Q. Wei, C. Liang, K. Wang, J. Guo, D. Zhao, B. Wang, R. Chen, G. Xing, J. Phys. Chem. Lett. 2020, 11, 5877.
- [46] K. Park, J.-H. Lee, J.-W. Lee, ACS Energy Lett. 2022, 7, 1230.
- [47] C. Liang, H. Gu, Y. Xia, Z. Wang, X. Liu, J. Xia, S. Zuo, Y. Hu, X. Gao, W. Hui, L. Chao, T. Niu, M. Fang, H. Lu, H. Dong, H. Yu, S. Chen, X. Ran, L. Song, B. Li, J. Zhang, Y. Peng, G. Shao, J. Wang, Y. Chen, G. Xing, W. Huang, Nat. Energy 2021, 6, 38.
- [48] T. Honda, A. Nakao, K. Ishihara, Y. Higaki, K. Higaki, A. Takahara, Y. Iwasaki, S.-I. Yusa, Polym. J. 2018, 50, 381.
- [49] W. Deng, X. Jin, Y. Lv, X. Zhang, X. Zhang, J. Jie, Adv. Funct. Mater. 2019, 29, 1903861.
- [50] A. Ren, H. Wang, L. Dai, J. Xia, X. Bai, E. Butler-Caddle, J. A. Smith, H. Lai, J. Ye, X. Li, S. Zhan, C. Yao, Z. Li, M. Tang, X. Liu, J. Bi, B. Li, S. Kai, R. Chen, H. Yan, J. Hong, L. Yuan, I. P. Marko, A. Wonfor, F. Fu, S. A. Hindmarsh, A. M. Sanchez, J. Lloyd-Hughes, S. J. Sweeney, A. Rao, et al., Nat. Photonics 2023, 17, 798.
- Y. Liu, C. Tao, Y. Cao, L. Chen, S. Wang, P. Li, C. Wang, C. Liu, F. Ye, S. Hu, M. Xiao, Z. Gao, P. Gui, F. Yao, K. Dong, J. Li, X. Hu, H. Cong, S.





www.advancedsciencenews.com

www.advopticalmat.de

21951071. 0. Downloaded from https://onlinelibrary.wiley.com/doi/10.1002/adom.202303051 by Zhejiang University, Wiley Online Library on [13/12/2023]. See the Terms and Conditions (https://onlinelibrary.wiley.com/terms

-and-conditions) on Wiley Online Library for rules of use; OA articles are governed by the applicable Creative Commons License

- Jia, T. Wang, J. Wang, G. Li, W. Huang, W. Ke, J. Wang, G. Fang, *Nat. Commun.* **2022**, *13*, 7425.
- [52] R. P. Shi, X. D. Huang, J. K. O. Sin, P. T. Lai, IEEE Electron Device Lett. 2016, 37, 1555.
- [53] A. Rashidi, M. Monavarian, A. Aragon, A. Rishinaramangalam, D. Feezell, IEEE Electron Device Lett. 2018, 39, 520.
- [54] W.-G. Li, X.-D. Wang, J.-F. Liao, Y. Jiang, D.-B. Kuang, Adv. Funct. Mater. 2020, 30, 1909701.